

Characterization of TiO₂ nanoparticles fluidization using X-ray imaging and pressure signals

Gómez-Hernández, Jesús; Sánchez-Delgado, Sergio; Wagner, Evert; Mudde, Robert F.; van Ommen, J. Ruud

DOI

[10.1016/j.powtec.2016.11.068](https://doi.org/10.1016/j.powtec.2016.11.068)

Publication date

2017

Document Version

Accepted author manuscript

Published in

Powder Technology

Citation (APA)

Gómez-Hernández, J., Sánchez-Delgado, S., Wagner, E., Mudde, R. F., & van Ommen, J. R. (2017). Characterization of TiO₂ nanoparticles fluidization using X-ray imaging and pressure signals. *Powder Technology*, 446-454. <https://doi.org/10.1016/j.powtec.2016.11.068>

Important note

To cite this publication, please use the final published version (if applicable). Please check the document version above.

Copyright

Other than for strictly personal use, it is not permitted to download, forward or distribute the text or part of it, without the consent of the author(s) and/or copyright holder(s), unless the work is under an open content license such as Creative Commons.

Takedown policy

Please contact us and provide details if you believe this document breaches copyrights. We will remove access to the work immediately and investigate your claim.

Characterization of TiO₂ nanoparticles fluidization using X-ray imaging and pressure signals

Jesús Gómez-Hernández ^{a*}, Sergio Sánchez-Delgado^a, Evert Wagner^b, Robert F. Mudde^b, J. Ruud van Ommen^b

^aCarlos III University of Madrid;

Avda. de la Universidad 30, 28911 Leganés, Madrid, Spain

^bDelft University of Technology;

Julianalaan 136, 2628BL Delft, The Netherlands

* T: +34-670470417; E: jegomez@ing.uc3m

ABSTRACT

The fluidization of TiO₂-P25 nanoparticles is characterized by studying the X-ray attenuation through the bed and the dynamic response of pressure fluctuations to the influence of the gas velocity. The X-ray results are based on a flat detector capable of measuring a 2D projection of the column from a height of 3 cm above the distributor to the freeboard. Pressure fluctuation signals are analyzed in the time and frequency domain. The strong influence of hysteresis when increasing or decreasing the gas flow is used in the experiments to compare a well fluidized state to channels formation. Thus, two experimental procedures were carried out changing the gas velocity. First, the gas flow is decreased changing from fully fluidized to packed bed. In the second type of tests, the gas velocity is increased from packed bed to well fluidized. The use of Digital Image Analysis (DIA) techniques to study the X-ray images show the homogeneous distribution of solids within the bed when the gas velocity is decreased. In these tests, a smooth fluidization is found up to a gas velocity of 3 cm/s, while higher gas flows change the bed state to vigorous fluidization. Pressure signals revealed that Baskakov's

frequency can be used to determine the regime of the bed, smooth or vigorous bubbling. Tests with poor fluidization show that the formation of channels modifies the bed structure, hindering to reach the fluidization quality of well fluidized tests for the same experimental conditions.

Keywords:

Fluidized bed, Nanoparticles, X-ray imaging, pressure fluctuations, hysteresis, channels

Nomenclature

C	intensity of the image
\bar{C}	averaged intensity map
D	column diameter
f	frequency
f_I	frequency peak I
f_{II}	frequency peak II
H	bed height
H_0	initial bed height
h_{free}	bed surface height
K	image index
N	number of images acquired
U_g	gas velocity

U_{mf} minimum fluidization velocity

X horizontal pixel position

Y vertical pixel position

Greek symbols

Δx horizontal gap between grid locations

Δy vertical gap between grid locations

σ standard deviation of the images

σ_p standard deviation of the pressure signal

Abbreviations

ABF Agglomerate Bubbling Fluidization

APF Agglomerate Particulate Fluidization

CE Cumulative Energy

DIA Digital Image Analysis

PSD Power Spectral Density

1. Introduction

Fluidization of nanoparticles is a good technique to handle and process large amounts of nanopowder. Nanoparticles fluidize forming micron-size agglomerates due to the strong interparticle forces between them [1, 2]. The dynamic equilibrium between cohesive and shear forces that suspend the

agglomerates determines the agglomerate size, and thus, influences on the fluidization state of the bed.

Fluidization of nanopowders can be classified in two fluidization regimes, Agglomerate Particulate Fluidization (APF) and Agglomerate Bubbling Fluidization (ABF) [3]. APF refers to a smooth and bubble-less fluidization with high bed expansion, while ABF is characterized by the presence of bubbles and low bed expansion [2, 3]. Focusing on ABF powders, there is a strong hysteresis effect in the determination of the minimum fluidization velocity [4 - 6]. When the gas flow is progressively increased from the initial packed bed state, the cohesive forces between agglomerates hamper the fluidization start. Channels are commonly formed near the column walls when the gas velocity is higher than the minimum fluidization velocity [3]. Only when channels collapse, the bed can be fluidized at relatively high gas velocities. A sudden increase of the gas velocity can lead to the particles fluidization, enabling the determination of the minimum fluidization velocity by decreasing the gas velocity. This procedure is more reproducible, and thus, it has been usually employed for the estimation of the minimum fluidization velocity independently of the particle size [7, 8].

A key parameter to assess the fluidization behaviour is the local solids distribution. The local solids distribution can help us to elucidate nanopowder behaviour as a function of the gas velocity. An attractive way to determine the gas and solids distribution within the bed is X-ray imaging or tomography. Previous studies showed its capability to characterize non-intrusively the fluidization behaviour for micron-sized particles [9 - 14]. In these works [9 - 14], 2 rows of 96 detectors were located around the column, measuring the X-rays attenuation at two heights. This experimental setup permitted the bubble size

estimation employing reconstruction algorithms [9, 15, 16]. However, in this study, these detectors have been replaced by a flat plate detector that measures the X-rays attenuation in one direction. Other works have studied nanoparticle fluidization employing radioactive techniques. Esmaeli et al. [6], used a radioactive densitometry to estimate the solids concentration over the cross-section of 5 cm inner diameter column. The results showed that zirconia and aluminium nanoparticles, ABF type, present a lower solid hold-up at lower positions of the bed, where the larger agglomerates were located. Similarly, Gundogdu et al. [17] used an X-ray microtomography system with high spatial resolution and fast radiographic imaging. They studied the nanoparticles behaviour in both 2D and 3D fluidized beds showing qualitative results of the bed structure after the increase of the gas velocity. Similarly, Jung et al. [18] showed solid volume fractions of 0.38% for 10 nm silica particles.

Although the X-ray system obtains valuable results, its use is not feasible to analyze industrial applications. Many measurement techniques have been developed to describe the dynamic phenomena occurring in the bed [19, 20]. Although the wide amount of measurements that can be used to describe the fluidization state, such as techniques based on optic fiber probes [21], laser measurements [22], acoustic emissions [23, 24], and bed conductance [25], the most commonly used technique is the pressure fluctuation measurements. The pressure-based measurement system is low-cost and straightforward to apply even under harsh industrial conditions [2]. In the literature, pressure drop has been employed to describe nanoparticles fluidization [2, 4, 6, 18, 26 - 28]. Only a few works have analyzed pressure fluctuation signals in detail. Tamadondar et al. [29] studied the frequency domain of pressure signals for SiO₂-ABF type nanoparticles. They observed three frequency peaks that increase its energy with

the gas velocity. Other researchers have employed the dominant frequency to analyze a rotary reactor coupled with an atomic layer deposition process [30]. Nevertheless, a detailed characterization of pressure signals in time and frequency domain is still missing for nanopowder fluidized beds, and specially, for channeling fluidization.

In this work, we characterize the fluidization of TiO₂ nanoparticles as a function of gas velocity using an X-ray imaging system and pressure fluctuation signals. The hysteresis effect described in previous papers for TiO₂ nanoparticles is used to compare proper fluidized behavior to channeling fluidization. Thus, two experimental approaches, increasing or decreasing gas velocity, are compared in detail. The results show the differences between them using both X-ray measurements and pressure signals.

2. Experimental setup

2.1. Experimental facility

The fluidized bed column consisted of a PMMA of 5 cm inner diameter and wall thickness of 5 mm. The air distributor used was a sintered bronze plate with pore sizes ranging from 30 to 70 μm , and a thickness of 7 mm. The column had a height of 1.5 m with freeboard placed on top of it to reduce the elutriation of nanoparticles. A mass of 12 grams TiO₂-P25 nanoparticles, with a density of $\rho_p = 4000 \text{ kg/m}^3$ and a mean diameter of 21 nm, were loaded for each experiment. High-purity nitrogen at ambient temperature was used to fluidize the bed. The gas velocity was operated using a mass flow controller. A two-stage water bubblers and HEPA filters were installed at the fluidizing gas outlet in order to prevent the emission of nanoparticles to the atmosphere.

A source-detector pair was used to measure the attenuation of the X-rays through the fluidized bed. The source was operated at 50 keV and 9 mA in order to achieve a high contrast between the dense and void phases within the bed [9]. The flat detector, Xineos-3131 CMOS model, consists of a 307 mm x 302 mm sensitive area with 1548 x 1524 pixel array. Each pixel has a size of 198 μm x 198 μm with 14 bits of pixel depth. The images were recorded at 22 Hz during 10 seconds.

Figure 1-a shows the sketch of the system while Fig. 1-b illustrates the projection of the column measured by the flat X-ray detector. As can be seen in Fig. 1-b, the region analyzed covers from 3 cm above the gas distributor to the bed surface. High attenuations are represented by cold colors (blue), such as the attenuation caused by the lead collimator located next to the source or the bolts placed at the column flanges. In contrast, hot colors (red) represent low values of X-ray attenuation, which point to a high gas phase concentration.

Figure 1. Experimental setup (a) with all the measurements in mm, and (b) measurement of the flat X-ray detector, $U_g = 15.3$ cm/s.

A piezoelectric pressure sensor, Kistler type 7261, was connected to the probe at 2 cm above the plenum. A fine mesh was installed in order to avoid any leak of nanoparticles into the probe. The differential pressure fluctuations were amplified using a Kistler amplifier type 50.515, which incorporates a low pass filter at 0.16 Hz and a high pass filter at 200 Hz. The signal was measured during 240 s using a sampling frequency of 400 Hz [31].

2.2. Experimental procedure

Prior to each experiment, the bed material was sieved using a 350 μm mesh in order to remove or break the storage agglomerates [3]. Then, the nanoparticles were gently poured into the column, which is defined as the initial reference state. Two different experiments were carried out changing the gas velocity. At first, the gas flow was increased up to 15.3 cm/s and gradually decreased up to the bed defluidization. In this case, the bed behavior changes from fully fluidized to packed bed since the cohesive forces between agglomerates are broken by the initial sudden increase of the gas flow. As we were decreasing the gas velocity (U_g), these experiments are referred as “high to low U_g ”. In the second type of tests, the gas velocity is increased from 0 to 15.3 cm/s. These experiments showed channeling for low gas velocities, while at higher gas velocities the bed is well fluidized. These tests are referred as “low to high U_g “. In both cases, a 5 minute pause was taken after each change of gas velocity before the measurements were started, so that the bed could stabilize. Furthermore, a new batch of nanoparticles were used after decreasing the gas velocity and after increasing the gas velocity. The bed mass was weighted before and after each experiments, finding a 3% of mass was lost due to NPs elutriation. Table 1 shows the nomenclature used for each experiment under different experimental conditions.

Table 1. Nomenclature for the experiments

2.3. Methods of analysis

As stated above, an X-ray imaging system was employed to characterize the fluidization behavior. With the use of Digital Image Analysis (DIA) the behavior within the fluidized bed can be determined, identifying not only if the fluidized bed

is fluidized, but also the quality of fluidization based on the homogeneity within the fluidized bed. Two techniques have been used for the images analyses:

-The images superposition in time: This technique reports the bubble pattern within the fluidized bed. An averaged intensity map ($\bar{C}_{x,y}$) in time is created as follows [32]:

$$\bar{C}_{x,y} = \frac{1}{N} \sum_{K=1}^N C_{x,y,K}$$

Where $C_{x,y,K}$ represents the intensity of the image, for each pixel position (X,Y) and N is the total images acquired for each case. The image superposition technique reports qualitative information related with the quality of fluidization for different cases.

-The standard deviation analysis for images: This technique is based on the calculation of the standard deviation of particle concentration for each pixel in the fluidized bed, as follows:

$$\sigma(x, y) = \left(\frac{\sum_{K=1}^N (C_{x,y,k} - \bar{C}_{x,y})}{N - 1} \right)^{0.5}$$

The standard deviation of pixel intensity reports the variability of the line-averaged particle concentration in time. Low values of the standard deviation represent regions where the presence of bubbles is very small or nonexistent. Regions with high presence of bubbles give a high value of standard deviation, due to the alternations between dilute and dense phase. Therefore, quantitative results can be reported using the standard deviation of the pixels, analyzing the excess gas effect in the fluidization quality. The standard deviations have been studied at 100 locations within the fluidized bed, which are defined as follows:

Figure 2. Grid used for the standard deviation analysis of pictures.

Where $\Delta x = D/11$; $\Delta y = h_{free}/11$ and h_{free} is the bed surface height, which is determined analyzing the X-ray pictures for each test. X and Y represent the location for each case, where X is the number of row and Y is the number of column $X \in [1,10]$, $Y \in [1,10]$.

Pressure fluctuation signals are analyzed in time and frequency domain [33]. In the time domain, the standard deviation (σ_p) characterizes the amplitude of the pressure signals, which can be used to identify a regime change or the bed defluidization for micron-sized particles [34 - 36]. It has been also employed to estimate the minimum fluidization velocity [7, 37], although it can be influenced by the gas velocity, making its application to industrial installations difficult [33]. In the frequency domain, the estimation of the power spectral density (PSD) gives information about the dominant frequencies present in the pressure signal [33]. In this way, it is possible to identify the fluidization regime and relate the PSD to physical phenomena [38 - 40]. Welch's method [41] is used to estimate the PSD function averaging 20 sub-spectra with a Hamming window. The energy contained in the power spectrum can also reflect a change in the fluidization state [35]. This variable, the cumulative energy (CE) represents the energy of the signal, and it will be estimated after the computation of the Welch's spectra.

3. Results and Discussion

The results show the different types of fluidization behavior of $\text{TiO}_2\text{-P25}$ nanoparticles when the bed is fluidized and the gas flow is stepwise decreased, or when the initial state is packed and the gas flow is stepwise increased. These tests are analyzed in detail employing the X-ray attenuation measurements and

the differential pressure sensors. First of all, X-ray measurements are analyzed using image techniques, focusing on the channeling and maldistribution detection. Later, pressure fluctuation signals are studied in both time and frequency domain in order to characterize each fluidization regime.

3.1 X-ray characterization

Figures 3 and 4 show the averaged intensity maps for both experimental procedures. The visual inspection of figures and movies (see supplementary data) gives a qualitative description of the fluidized state. The low attenuations of X-rays are represented by hot colors (red) and are related to the presence of high gas concentrations. The high attenuations present cold colors (blue) pointing to high solid concentrations.

Figure 3: Averaged intensity maps for stepwise decreasing the gas velocity. Cases “m” to “a”.

As can be observed in Fig. 3 when decreasing the gas velocity from high to low U_g , the X-ray attenuation through the bed is quite symmetric and homogeneous. This result points to smooth fluidization behavior where no preferential gas path is observed for all gas velocities. Clearly, all experiments were well fluidized.

It is worth to point out the appearance of a high attenuation zone around the column center for low gas velocities, Fig. 3-a/b/c/d. In these cases, the longer path length at the bed center increases the attenuation of the X-rays, and thus, the flat X-ray detector measures low energies. As the gas flow is increased, Fig. 3-h/i/j, the presence of bubbles in the center of the fluidized bed also increases, and thus, the amount of material detected in that region is lower [42].

Figure 4. Averaged intensity maps when increasing the gas velocity. Cases “A” to “M”.

On the other hand, experiments from low to high U_g show internal structures within the fluidized bed. For tests A to D, the large cohesive forces between agglomerates tend to prevent the appearance of bubbles [2]. However, the gas flows through small channels slightly increasing the bed expansion [43, 44]. As the gas flow is increased, some channels appear near the walls, Fig. 4-F to J. Obviously, this non-uniform distribution of gas across the section generates dead regions at the right side of the column.

When the gas flow is increased, Fig. 4-J/K, the particles at the sides of the channels or on the top of the bed start to be fluidized, breaking the channels [3]. A uniform distribution of the excess gas through the reactor is reached. At these fluidizing velocities, the bed is well fluidized, showing an attenuation map that is similar to Fig. 3-k/l/m.

The estimation of the bed height, which is difficult by visual inspection, can be clearly done analyzing the X-ray pictures. Figure 5 presents the evolution of the bed expansion ratio (H/H_0) as a function of the gas velocity for both experimental procedures. The values plotted in this figure have been obtained averaging several experiments. Three zones can be detected when decreasing the gas velocity in Fig. 5. The analysis of Fig. 3 together with the study of all X-ray images show three different regimes that could be classified within the multiple bubble regime described by Johnsson et al. [35] for Geldart B particles (see the movies in the supplementary material):

- From $U_g = 0$ to 3 cm/s:

There is a continuous passage of small bubbles through the bed. The bed shows a smooth fluidization with multiple bubbles exploding at the bed surface.

- From $U_g = 3$ to 7 cm/s:

Large bubbles coalesce rapidly through the bed. A vigorous fluidization can be seen in the movies.

- From $U_g = 7$ to 15 cm/s:

The violent bubble eruptions at the top of the bed make difficult to define the bed surface. Nevertheless, the bed is not under transport conditions.

The results shown in Figs. 3 and 5 define the minimum fluidization velocity (U_{mf}) when the bed expansion ratio values reach a plateau. This value, $U_{mf} = 4$ cm/s, is in agreement with previous results of Tahmasebpour et al. [27], who measured the bed pressure drop and the bed expansion ratio to determine U_{mf} .

Fig. 5 shows that when increasing the gas velocity, only a proper fluidization is shown at the highest gas velocities. This hysteresis effect has been reported before [6, 44]. Also, it is worth to note that, in this case, the bed cannot reach the same bed expansion ratio as for the previous experimental procedure. This could be explained by the change of the agglomerates during the fluidization at low gas velocities, when channels were formed.

Figure 5. Bed expansion ratio as a function of the gas velocity.

The standard deviation of the images is computed to describe quantitatively the fluidization regimes. As stated above, high standard deviation values will point to large fluctuations of the solid concentration. To relate the bed fluctuations caused

by the bubbles with the bed expansion, standard deviation values are normalized by the bed expansion results shown in Fig. 5. In this way, the information local phenomena and bed behavior are described in one plot. Figure 6 presents the normalized standard deviation values considering a matrix of $X \times Y = 10 \times 10$ points equally located between the bed surface, column walls and bottom of the bed, as was depicted in Fig. 2. In this way, the entire bed is considered in the results. A distribution of normalized standard deviation values is plotted for each gas velocity using boxplots. In the figure, outliers are plotted in red while the median, quartiles and extremes values of each distribution are plotted in blue.

Figure 6. Normalized standard deviation of solid concentration analyzing the entire bed ($X \times Y = 10 \times 10$). (a) Decreasing the gas velocity, (b) increasing the gas velocity.

Regarding the well fluidized tests Fig. 6-a, the median values of the normalized standard deviation increase with the gas velocity due to the increase of the number and size of the bubbles, and the bed expansion. Also, the shape of the distribution reflects whether the bed is homogeneously distributed. For all tests shown in Fig. 6-a, the distributions presented a regular shape with the median in the center. This result suggests a homogeneous fluidization in the entire bed, which is in agreement with the qualitative results, Fig. 3. Comparing between low and high gas velocities, wider distributions are obtained at higher gas velocities. Therefore, a higher number of fluctuations are detected at high gas velocities, which are caused by a larger number of bubbles in the bed. Two main regions can be found: (i) from $U_g = 0$ to 3 cm/s narrow distributions point to a smooth fluidization without great changes in the bed concentration, and (ii) from $U_g = 3$ to 15.3 cm/s wide distributions identify a vigorous fluidization. The third region

identified using the bed expansion results, Fig. 5, cannot be clearly seen in Fig. 6-a. It is worth to point out that the width of these distributions is roughly constant from $U_g = 3.4$ cm/s up to $U_g = 11.88$ cm/s. From $U_g = 11.88$ to 15.3 cm/s the distribution is wider pointing to a more vigorous bubbling bed.

For the low to high U_g experiments, low gas velocities showed narrow distributions with low median values; see Fig. 6-b. Regarding the low gas velocities up to $U_g = 2.55$ m/s, no significant differences are found between both experiment types (Fig. 6-a and 6-b). The presence of channels from $U_g = 5.1$ to 10.18 cm/s leads to uneven distributions with lower median values than those shown in Fig. 6-a. Only when the channels are broken and the bed is fluidized, from $U_g = 11.88$ to 15.3 cm/s, the distributions showed normal shape with similar median values.

Concerning on the uneven distributions, it is possible to detect the channels studying the standard deviation values at the bed center. Figure 7 gives the standard deviation values as a function of the horizontal position for tests at $U_g = 10.18$, 11.88 and 13.6 cm/s at the center of the bed. High values are obtained for $U_g = 11.88$ and 13.6 cm/s (cases K and L) through the cross section of the bed since the bed is well fluidized. However, the presence of a channel near the column wall (Fig. 4-J) is detected as a region with high standard deviation values, Fig. 7. The rest of the bed is not fluidized, as reflected by the low standard deviation values. Thus, this explains the uneven distribution of standard deviation values produced by the channels.

Figure 7. Standard deviation of the images at the center of the bed when decreasing the gas velocity.

3.2 Pressure fluctuation analysis

The use of pressure fluctuation signals to characterize the fluidization regimes has been widely applied for micron-sized particles. However, the low density of the agglomerates and the small bubble size makes the characterization of the nano-fluidization using pressure fluctuations more challenging [29]. Using the pressure analysis, we can also try to discriminate between good fluidization and channeling. The results of such different fluidization behaviors are characterized studying the pressure signals in both time and frequency domain. Results of experiments at $U_g = 1.3, 2.55, 6.8$ and 11.88 cm/s are studied in detail. These velocities have been chosen according to the different fluidization regimes identified in Fig. 5.

Pressure signals recorded during good fluidization behavior at different gas velocities are presented in Fig. 8. All the signals show a small amplitude and a strong periodicity. The shape of the signals, especially at low gas velocities Fig. 8-a/b, is similar to the pressure signal that defines the multiple bubble regime of micron-sized particles [35]. At higher gas velocities higher amplitude and more fluctuations are shown, although the signal shape is similar, Fig. 8-c/d.

Figure 8. Pressure time-series measured decreasing the gas flow: (a) $U_g = 1.3$ cm/s, (b) $U_g = 2.55$ cm/s, (c) $U_g = 6.8$ cm/s and (d) $U_g = 11.88$ cm/s.

The standard deviation values of pressure signals are presented for both experimental procedures in Figure 9. Under good fluidization conditions (high to low U_g), the standard deviation shows a nearly linear decay from high gas velocities up to $U_g = 3$ cm/s. For these gas velocities, the bed is well fluidized. However, a different trend is shown for gas velocities below $U_g = 3$ cm/s. In these

experiments, the bed is near minimum fluidization conditions and the small bubbles cause the low standard deviation values. Also, it is worth to point out the similar trend of the image standard deviation, Fig. 6-a, and the standard deviation of the pressure signal, Fig. 9.

Similar standard deviation values are obtained near minimum fluidization velocity for both experimental procedures. However, when increasing the velocity (low to high U_g), the bed is not fluidized, as was shown in Fig. 4. For even higher gas velocities, the presence of channels increases the fluctuations of the pressure signals, which is reflected as high standard deviation values, Fig. 9. As the channels increase the superficial velocity of the gas leaving the bed, higher amplitudes are recorded in the pressure signal [45]. Only when the bed is completely fluidized at the highest gas velocities, standard deviation values are similar for both procedures. Therefore, the high influence of the superficial gas velocity on the standard deviation hinders its application to ABF nano-fluidization even for low gas velocities.

Figure 9. Standard deviation of pressure fluctuation signals.

Figure 10 shows the power spectra of both approaches for different velocities. Focusing on the well fluidized tests, two main frequency peaks are shown at $f_I = 2.4$ Hz and $f_{II} = 4.5$ Hz for low gas velocity, Fig.10-a. As the gas velocity increases, the energy at $f_{II} = 4.5$ Hz is progressively reduced until it disappears at $U_g = 11.88$ cm/s, while the peak related to the bulk movement of the bed (f_I) remains fairly constant, Fig. 10-d. The second frequency peak (f_{II}) is equal to the Baskakov's frequency for the experimental conditions used. Baskakov showed that this frequency is related to the bubble eruption at the bed surface [40]. Thus, the disappearance of the second frequency peak points to the reduction of the

surface waves influence on the power spectra. Following the regime description explained before (Figs. 3 and 5), the bubble eruption on the bed surface change significantly with the gas velocity increase. Therefore, the progressive disappearance of f_{II} could be used to determine the fluidization regime.

Regarding the experiments with channels, significant differences can be seen for all velocities when comparing to the corresponding well fluidized state. For $U_g = 1.3$ cm/s Fig. 10-a, the peak frequency is detected at low frequencies although another frequency peak is shown around the bed frequency. In Fig. 10-b, a frequency peak is also shown near f_{II} . However, the frequency peak related to the bed behavior is moved to lower frequencies, suggesting a change in the long-term behavior of the bed. The formation of channels causes the appearance of frequency peaks at higher frequencies, Fig. 10-c, which is in agreement with previous studies using micron-sized particles [47]. Once the bed is fluidized, the bed frequency is shown near f_I , although some significant differences can be seen around $f = 6$ and 10 Hz.

Figure 10. Power spectrum of pressure signals for both experimental procedures. (a) $U_g = 1.3$ cm/s, (b) $U_g = 2.6$ cm/s, (c) $U_g = 6.8$ cm/s, (d) $U_g = 11.9$ cm/s.

The cumulative energy distribution of the PSD is computed in Figure 11 to further analyze the energy within the signal. The plot of well fluidized tests, Fig. 11-a, shows that the energy is mainly distributed between f_I and f_{II} . Only when there is a vigorous fluidization and the bed surface is difficult to define at $U_g = 11.88$ cm/s, the energy is equally distributed between low frequencies, f_I and high frequencies. In contrast, the energy distribution for the experiments with stepwise increasing gas velocity present a different result; see Fig. 11-b. For low gas

velocities, the energy is distributed within the low frequency domain. Once channels are formed at $U_g = 6.8$ cm/s, the energy distribution is similar to the energy distribution when the bed is fluidized at $U_g = 11.88$ cm/s, Fig. 11-b. The main difference between them can be seen at frequencies below f_i .

The comparison between Fig. 11-a to Fig. 11-b for each velocity shows that the increasing procedure is not able to reach the same fluidization state as when the gas flow is decreased. This result was also previously shown using the image analysis of the X-ray results. Also, it is interesting to note that the fluctuations caused by channels (Fig.11-b $U_g = 6.8$ cm/s), where some particles are fluidized at the top of the bed, encode the signal energy near to the fluidized state of $U_g = 2.6$ cm/s in Fig. 11-a. This suggests that the cumulative energy distribution of the PSD could be also used to determine the fluidization regime.

Figure 11. Cumulative energy distribution of the PSD for both experimental procedures. (a) High to low U_g , (b) low to high U_g .

4. Conclusions

Fluidization behavior of TiO_2 -P25 nanoparticles has been characterized using an X-ray imaging system and pressure fluctuation signals. Both techniques were able to describe the fluidization regimes. A high hysteresis effect has been shown depending on the fluidization procedure. On one hand, when decreasing gas velocity, homogeneous fluidization was achieved showing smooth and vigorous fluidization at low and high gas velocities, respectively. On the other hand, the increase of gas velocity from the packed bed state caused the formation of channels through the bed. At the highest velocities the bed was well fluidized but showing lower bed expansion compared to the previous approach.

The image analysis of X-ray results identified two clear regimes studying the bed height expansion and the standard deviation of the images for well fluidized tests: (i) a smooth fluidization regime for low gas velocities, up to $U_g = 3$ cm/s, where small bubbles are shown, and (ii) a vigorous fluidization regimes for higher gas velocities. The presence of channels and maldistributions of particles inside the bed can be detected estimating the average and the standard deviation of the images. Channels caused the uneven distribution of standard deviation values within the bed. Nevertheless, when the channels collapse at higher gas velocities, the bed is homogeneously fluidized.

Pressure characterization in the time domain has been carried out estimating the standard deviation of the signals. This method is highly influenced by the superficial gas velocity, as was clearly seen when channels were formed. The standard deviation at low gas velocities for both types of experiments showed similar values, even though the fluidization state was completely different. Thus, this method is not recommended to analyze nanopowder fluidization.

The analysis of the pressure signals in the frequency domain can describe the fluidization regimes and the presence of channels. For good fluidization tests, the power spectral density identified the multiple bubble regime. Baskakov's frequency can be used to determine whether the bed is at the smooth or vigorous fluidization regime. The regimes identified using the X-ray results are in agreement with pressure analysis. Channels cause the codification of the power spectra in different frequencies. After the channels breakage, the energy of the PSD is distributed in a different way, pointing to a different bed structure compared to well fluidized tests.

REFERENCES

- [1] J.P.K. Seville, C.D. Willett, P.C. Knight, Interparticle forces in fluidisation: A review, *Powder Technol.* 113 (2000) 261-268.
- [2] J.R. van Ommen, J. Manuel Valverde, R. Pfeffer, Fluidization of nanopowders: a review, *J. Nanoparticle Res.* 14 (2012) 737.
- [3] Y. Wang, G.S. Gu, F. Wei, J. Wu, Fluidization and agglomerate structure of SiO₂ nanoparticles, *Powder Technol.* 124 (2002) 152-159.
- [4] C. Zhu, Q. Yu, R.N. Dave, R. Pfeffer, Gas fluidization characteristics of nanoparticle agglomerates, *AIChE J.* 51 (2005) 426-439.
- [5] H. Yu, Q. Zhang, G. Gu, Y. Wang, G. Luo, F. Wei, Hydrodynamics and gas mixing in a carbon nanotube agglomerate fluidized bed, *AIChE J.* 52 (2006) 4110-4123.
- [6] B. Esmaeili, J. Chaouki, C. Dubois, An evaluation of the solid hold-up distribution in a fluidized bed of nanoparticles using radioactive densitometry and fibre optics, *Can. J. Chem. Eng.* 86 (2008) 543-552.
- [7] D. Wilkinson, Determination of Minimum Fluidization Velocity by Pressure Fluctuation Measurement, *Can. J. Chem. Eng.* 73 (1995) 562-565.
- [8] C. Lin, M. Wey, S. You, The effect of particle size distribution on minimum fluidization velocity at high temperature, *Powder Technol.* 126 (2002) 297-301.
- [9] R.F. Mudde, Time-resolved X-ray tomography of a fluidized bed, *Powder Technol.* 199 (2010) 55-59.
- [10] R.F. Mudde, Bubbles in a fluidized bed: A fast X-ray scanner, *AIChE J.* 57 (2011) 2684-2690.

- [11] T.J. Heindel, A Review of X-Ray Flow Visualization With Applications to Multiphase Flows, *Journal of Fluids Engineering*. 133 (2011) 074001-074001.
- [12] G.C. Brouwer, E.C. Wagner, J.R. van Ommen, R.F. Mudde, Effects of pressure and fines content on bubble diameter in a fluidized bed studied using fast X-ray tomography, *Chem. Eng. J.* 207–208 (2012) 711-717.
- [13] J. Saayman, W. Nicol, J.R. Van Ommen, R.F. Mudde, Fast X-ray tomography for the quantification of the bubbling-, turbulent-and fast fluidization-flow regimes and void structures, *Chem. Eng. J.* 234 (2013) 437-447.
- [14] S. Maurer, E.C. Wagner, J.R. van Ommen, T.J. Schildhauer, S.L. Teske, S.M.A. Biollaz, A. Wokaun, R.F. Mudde, Influence of vertical internals on a bubbling fluidized bed characterized by X-ray tomography, *Int. J. Multiph. Flow*. 75 (2015) 237-249.
- [15] J. Gómez-Hernández, J. Ruud van Ommen, E. Wagner, R.F. Mudde, A fast reconstruction algorithm for time-resolved X-ray tomography in bubbling fluidized beds, *Powder Technol.* 290 (2016) 33-44.
- [16] X. Yang, J.R. van Ommen, R.F. Mudde, Comparison of genetic algorithm and algebraic reconstruction for X-ray tomography in bubbling fluidized beds, *Powder Technol.* 253 (2014) 626-637.
- [17] O. Gundogdu, P.M. Jenneson, U. Tuzun, Nano particle fluidisation in model 2-D and 3-D beds using high speed X-ray imaging and microtomography, *J. Nanopart. Res.* 9 (2007) 215-223.
- [18] J. Jung, D. Gidaspow, Fluidization of nano-size particles, *J. Nanopart. Res.* 4 (2002) 483-497.

- [19] J. Werther, Measurement techniques in fluidized beds, *Powder Technol.* 102 (1999) 15-36.
- [20] J.R. van Ommen, R. F. Mudde, Measuring the gas-solids distribution in fluidized beds-a review. *Int. J. Chem. Reactor Eng.* 6 (2008) 1-29.
- [21] G. Amos, J.M. Rhodes, H. Benkreira, Calculation of optic fibres calibration curves for the measurement of solids volume fractions in multiphase flows. *Powder Technol.* 88 (1996) 107-121.
- [22] J.V. Briongos, J.G. Soler, Free top fluidized bed surface fluctuations as a source of hydrodynamic data, *Powder Technol.* 134 (2002) 133-144.
- [23] C.A. Herrera, E. K. Levy, J. Ochs, Characteristics of acoustic standing waves in fluidized beds, *AIChE J.* 48 (2002) 503-513.
- [24] L. de Martin, J.V. Briongos, J.M. Aragon, M. C. Palancar, Can low frequency accelerometry replace pressure measurements for monitoring gas-solid fluidized beds? *Chem. Eng. Sci.* 65 (2010) 4055-4064.
- [25] F. Portoghese, P. House, F. Berruti, C. Briens, K. Adamiak, E. Chan, Electric conductance method to study the contact of injected liquid with fluidized particles, *AIChE J.* 54 (2008) 1770–1781.
- [26] L.F. Hakim, J.L. Portman, M.D. Casper, A.W. Weimer, Aggregation behavior of nanoparticles in fluidized beds, *Powder Technol.* 160 (2005) 149-160.
- [27] M. Tahmasebpour, L. de Martin, M. Talebi, N. Mostoufi, J.R. van Ommen, The role of the hydrogen bond in dense nanoparticle-gas suspensions, *Phys. Chem. Chem. Phys.* 15 (2013) 5788-5793.

- [28] S.W. Jeong, J.H. Lee, J. Kim, D.H. Lee, Fluidization behaviors of different types of multi-walled carbon nanotubes in gas-solid fluidized beds, *J. Ind. Eng. Chem.* 35 (2016) 217-223.
- [29] M.R. Tamadondar, R. Zarghami, M. Tahmasebpoor, N. Mostoufi, Characterization of the bubbling fluidization of nanoparticles, *Particuology* 16 (2014) 75-83.
- [30] C.-. Duan, X. Liu, B. Shan, R. Chen, Fluidized bed coupled rotary reactor for nanoparticles coating via atomic layer deposition, *Rev. Sci. Instrum.* 86 (2015).
- [31] J.R. van Ommen, J.C. Schouten, M.L.M. vanderStappen, C.M. van den Bleek, Response characteristics of probe-transducer systems for pressure measurements in gas-solid fluidized beds: how to prevent pitfalls in dynamic pressure measurements, *Powder Technol.* 106 (1999) 199-218.
- [32] S. Sánchez-Delgado, C. Marugán-Cruz, A. Soria-Verdugo, D. Santana, Estimation and experimental validation of the circulation time in a 2D gas-solid fluidized beds, *Powder Technol.* 235 (2013) 669-676.
- [33] J.R. van Ommen, S. Sasic, J. van der Schaaf, S. Gheorghiu, F. Johnsson, M. Coppens, Time-series analysis of pressure fluctuations in gas-solid fluidized beds - A review, *Int. J. Multiphase Flow.* 37 (2011) 403-428.
- [34] J. Gómez-Hernández, A. Soria-Verdugo, J.V. Briongos, D. Santana, Fluidized bed with a rotating distributor operated under defluidization conditions, *Chem. Eng. J.* 195–196 (2012) 198-207.

- [35] F. Johnsson, R.C. Zijerveld, J.C. Schouten, C.M. van den Bleek, B. Leckner, Characterization of fluidization regimes by time-series analysis of pressure fluctuations, *Int. J. Multiphase Flow*. 26 (2000) 663-715.
- [36] J.R. van Ommen, R.J. de Korte, C.M. van den Bleek, Rapid detection of defluidization using the standard deviation of pressure fluctuations, *Chem. Eng. Process*. 43 (2004) 1329-1335.
- [37] C.A.S. Felipe, S.C.S. Rocha, Prediction of minimum fluidization velocity of gas-solid fluidized beds by pressure fluctuation measurements - Analysis of the standard deviation methodology, *Powder Technol*. 174 (2007) 104-113.
- [38] J. van der Schaaf, J.C. Schouten, F. Johnsson, C.M. van den Bleek, Non-intrusive determination of bubble and slug length scales in fluidized beds by decomposition of the power spectral density of pressure time series, *Int. J. Multiphase Flow*. 28 (2002) 865-880.
- [39] H. Kage, M. Agari, H. Ogura, Y. Matsuno, Frequency analysis of pressure fluctuation in fluidized bed plenum and its confidence limit for detection of various modes of fluidization, *Adv. Powder Technol*. 11 (2000) 459-475.
- [40] H.T. Bi, A critical review of the complex pressure fluctuation phenomenon in gas-solids fluidized beds, *Chem. Eng. Sci*. 62 (2007) 3473-3493.
- [41] P. Welch, The use of fast Fourier transform for the estimation of power spectra, *IEEE Transactions Audio and Electroacoustics*. 15 (1967) 70-73.
- [42] J. Saayman, W. Nicol, J.R. Van Ommen, R.F. Mudde, Fast X-ray tomography for the quantification of the bubbling-, turbulent- and fast fluidization-flow regimes and void structures, *Chem. Eng. J*. 234 (2013) 437-447.

- [43] W. Yao, G. Guangsheng, W. Fei, W. Jun, Fluidization and agglomerate structure of SiO₂ nanoparticles, Powder Technol. 124 (2002) 152-159.
- [44] C. Zhu, Q. Yu, R.N. Dave, R. Pfeffer, Gas fluidization characteristics of nanoparticle agglomerates, AIChE J. 51 (2005) 426-439.
- [45] L. de Martin, K. van den Dries, J.R. van Ommen, Comparison of three different methodologies of pressure signal processing to monitor fluidized-bed dryers/granulators, Chem. Eng. J. 172 (2011).
- [46] A.P. Baskakov, V.G. Tuponogov, N.F. Filippovsky, A Study of Pressure-Fluctuations in a Bubbling Fluidized-Bed, Powder Technol. 45 (1986) 113-117.
- [47] J. Gómez-Hernández, J. Sanchez-Prieto, J. Villa Briongos, D. Santana, Wide band energy analysis of fluidized bed pressure fluctuations signals using frequency a division methodology, Chem. Eng. Sci. 105 (2014) 92-103.

List of figures

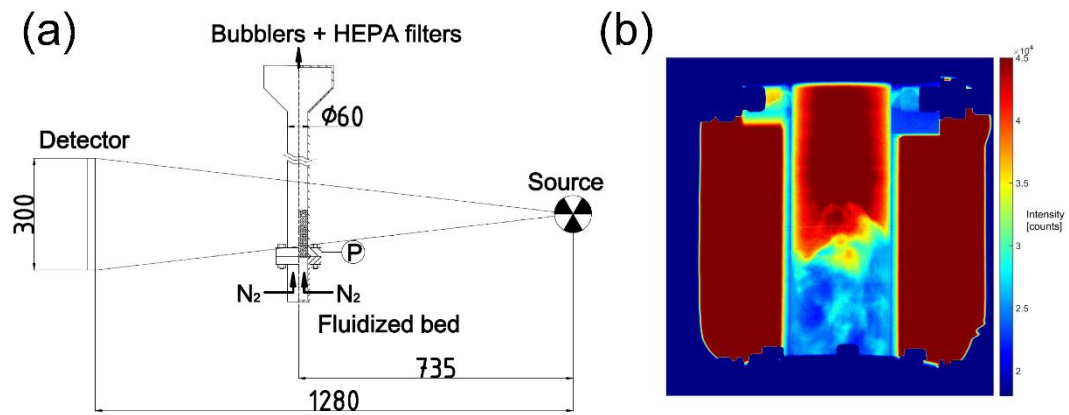


Figure 1. Experimental setup (a) with all the measurements in mm, and (b) measurement of the flat X-ray detector, $U_g = 15.3$ cm/s.

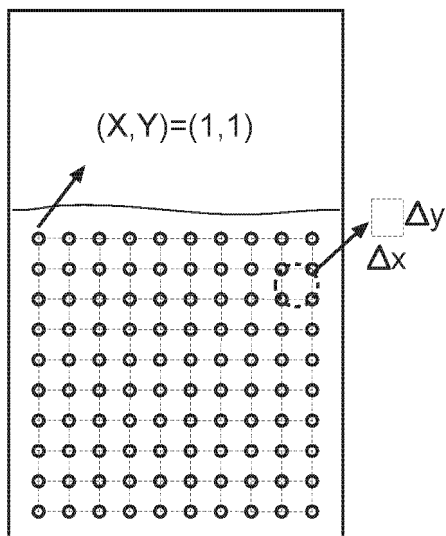


Figure 2. Grid used for the standard deviation analysis of pictures.

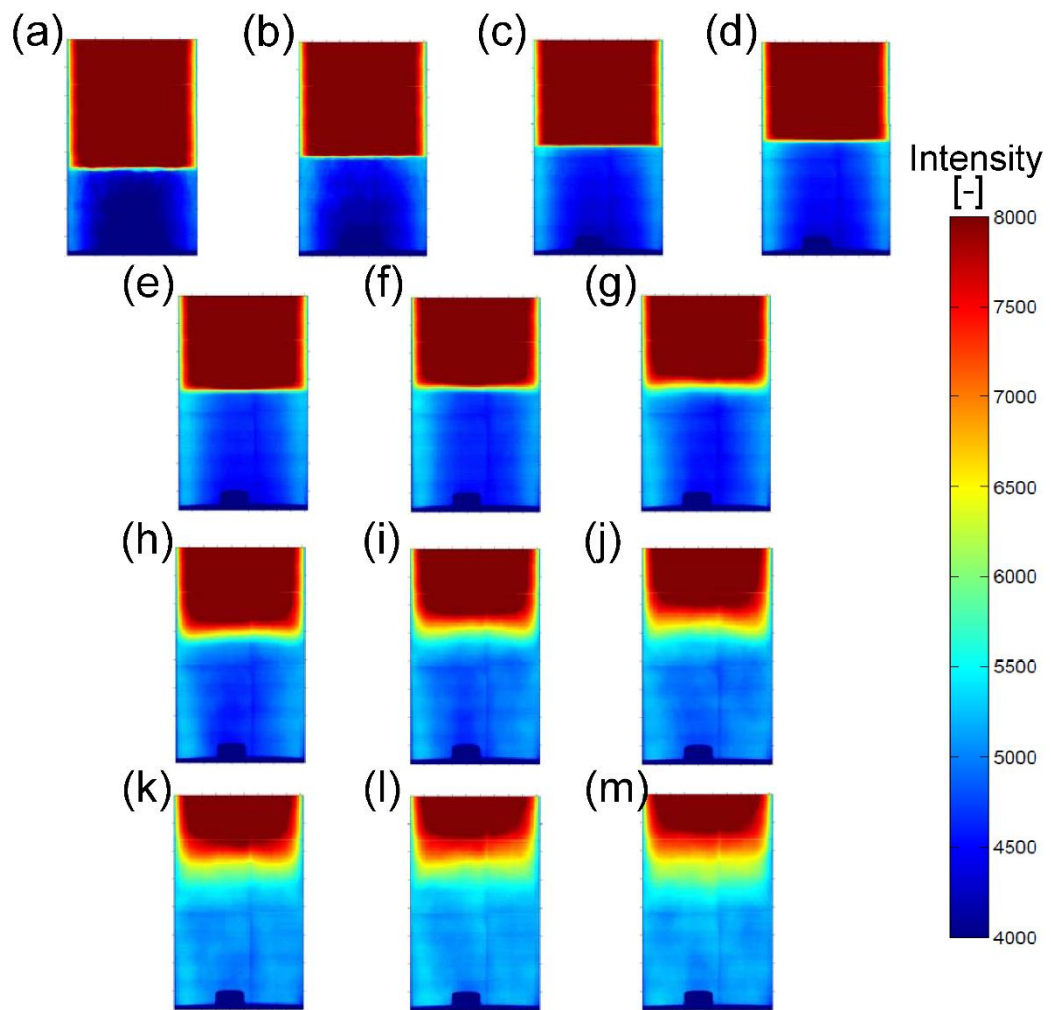


Figure 3: Averaged intensity maps for stepwise decreasing the gas velocity. Cases “m” to “a”.

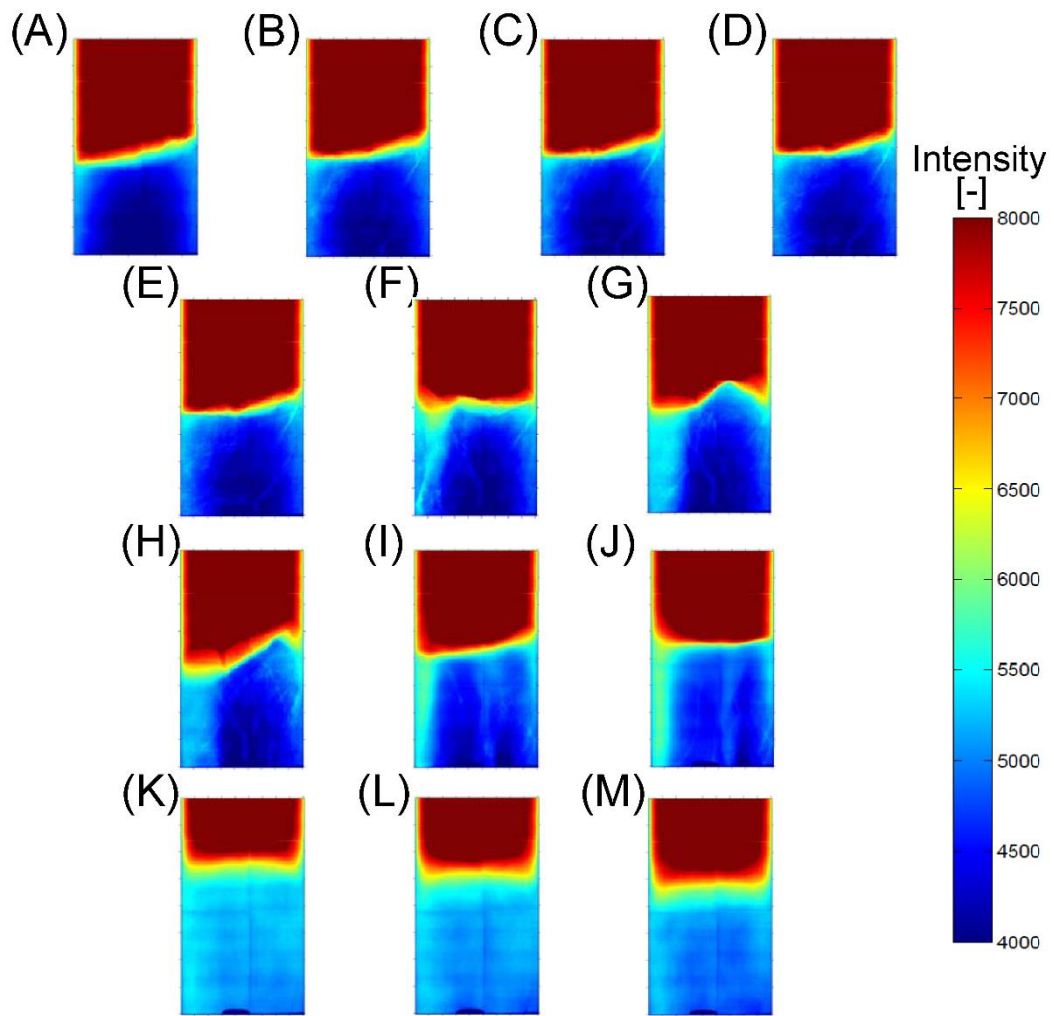


Figure 4. Averaged intensity maps when increasing the gas velocity. Cases “A” to “M”.

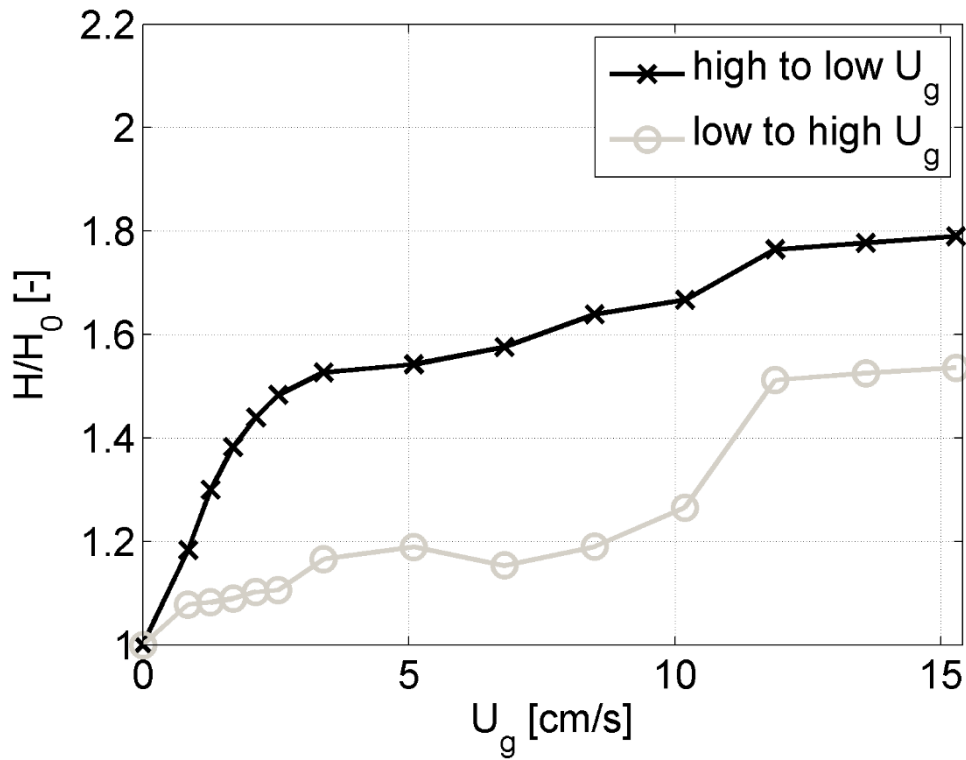


Figure 5. Bed expansion ratio as a function of the gas velocity.

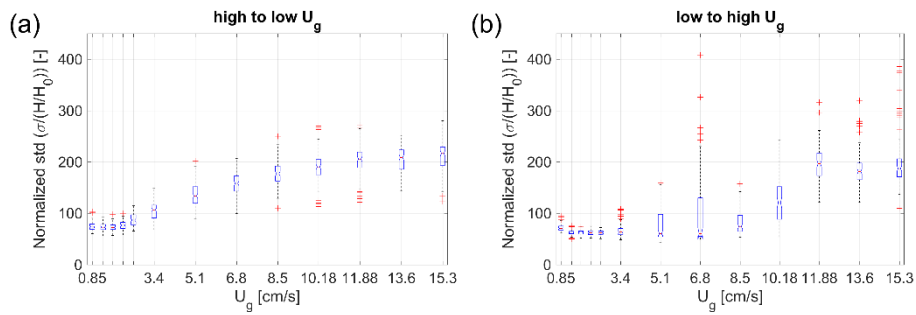


Figure 6. Normalized standard deviation of solid concentration analyzing the entire bed ($X \times Y = 10 \times 10$). (a) Decreasing the gas velocity, (b) increasing the gas velocity.

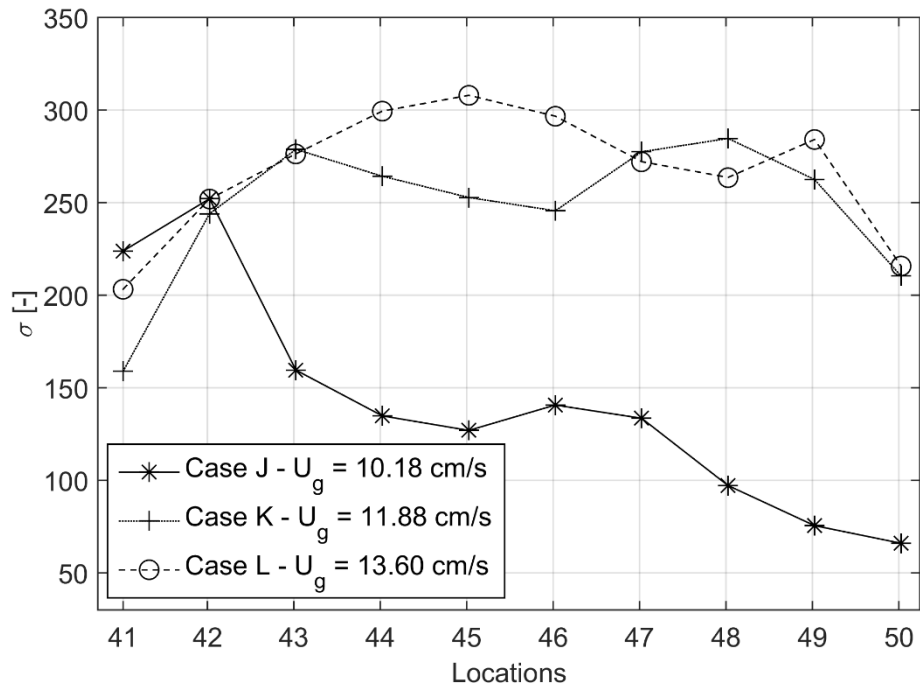


Figure 7. Standard deviation of the images at the center of the bed when decreasing the gas velocity.

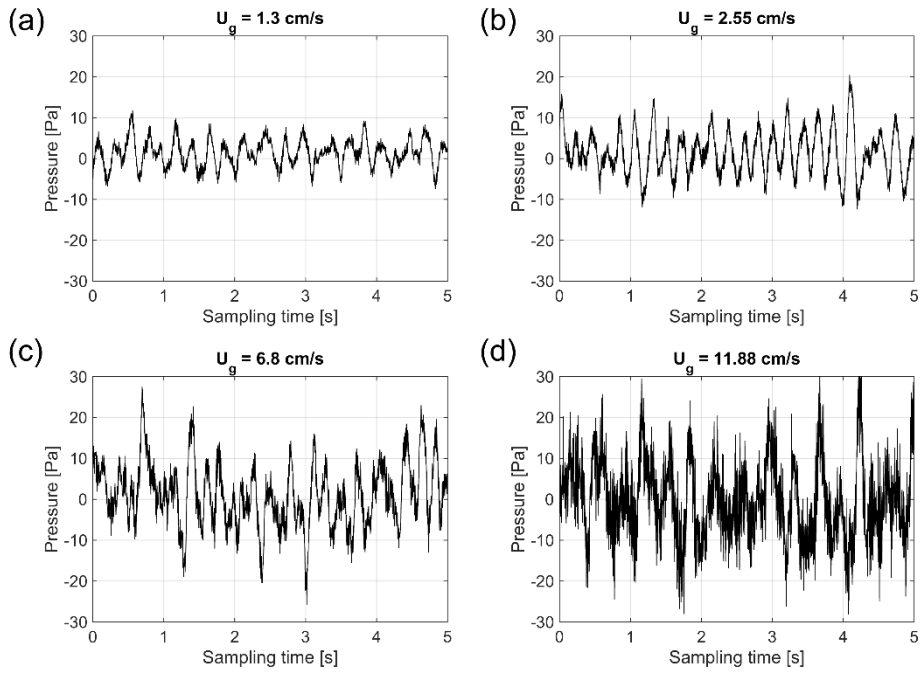


Figure 8. Pressure time-series measured decreasing the gas flow: (a) $U_g = 1.3$ cm/s, (b) $U_g = 2.55$ cm/s, (c) $U_g = 6.8$ cm/s and (d) $U_g = 11.88$ cm/s.

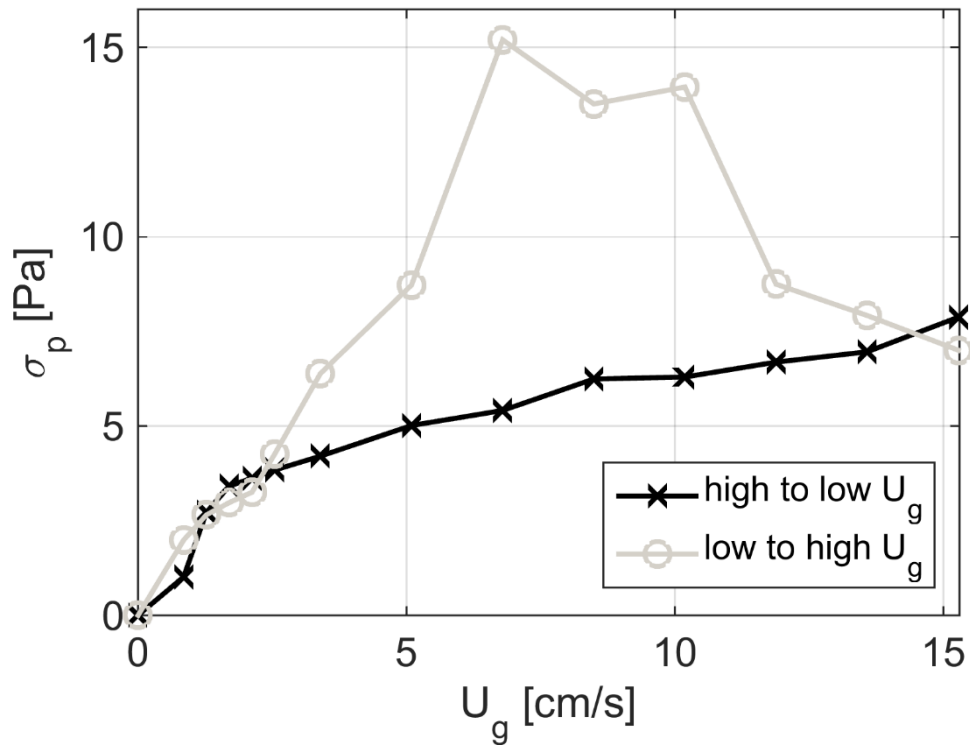


Figure 9. Standard deviation of pressure fluctuation signals.

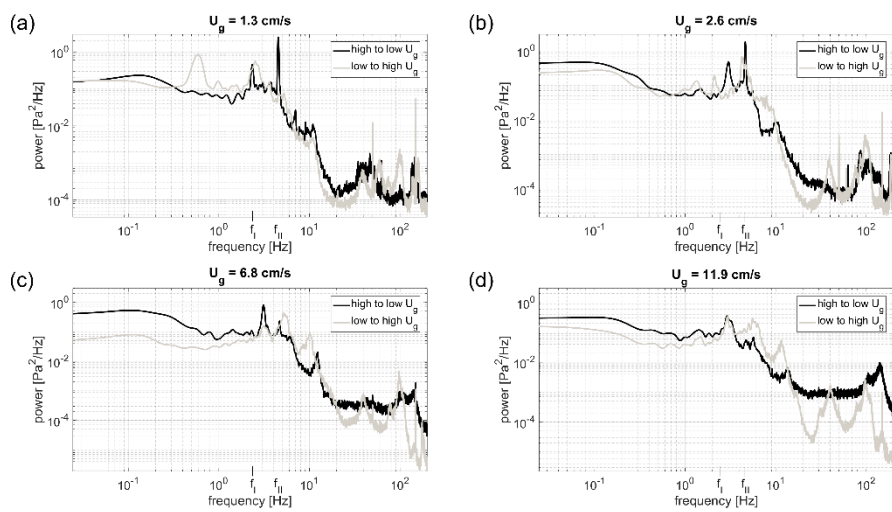


Figure 10. Power spectrum of pressure signals for both experimental procedures. (a) $U_g = 1.3$ cm/s, (b) $U_g = 2.6$ cm/s, (c) $U_g = 6.8$ cm/s, (d) $U_g = 11.9$ cm/s.

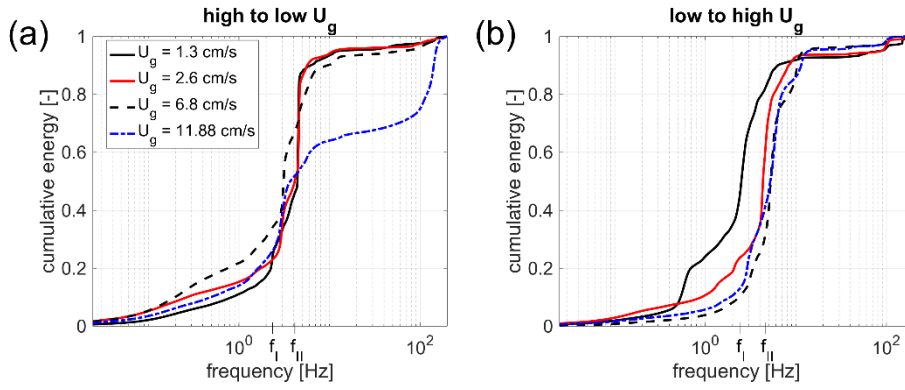


Figure 11. Cumulative energy distribution of the PSD for both experimental procedures. (a) High to low U_g , (b) low to high U_g .

List of tables

Table 1. Nomenclature for the experiments

	Excess gas, U_g [cm/s]												
	0.85	1.3	1.7	2.12	2.55	3.4	5.1	6.8	8.5	10.18	11.88	13.6	15.3
High to low U_g	a	b	c	d	e	f	g	h	i	j	k	l	m
Low to high U_g	A	B	C	D	E	F	G	H	I	J	K	L	M